

Towards a holistic magnetic braking model – II: explaining several long-term internal- and surface-spin properties of solar-like stars and the Sun

Arnab Sarkar¹★, Patrick Eggenberger², Lev Yungelson³ and Christopher A. Tout¹†

¹*Institute of Astronomy, The Observatories, Madingley Road, Cambridge CB3 0HA, UK*

²*Département d'Astronomie, Université de Genève, Versoix, Switzerland*

³*Institute of Astronomy of the Russian Academy of Sciences, 48 Pyatnitskaya Str., 119017 Moscow, Russia*

Accepted XXX. Received YYY; in original form ZZZ

ABSTRACT

We extend our model of magnetic braking (MB) from fully convective M-dwarfs (FCMDs) to explain the surface and internal spin P_{spin} evolution of partly convective dwarfs (PCDs) starting from disc-dispersal stage to main-sequence turnoff. In our model, the spin of the core is governed by shear at the core-envelope boundary while the spin of the envelope is governed by MB and shear. We show that (1) the most massive FCMDs experience a stronger spin-down than PCDs and less massive FCMDs; (2) the stalled spin-down and enhanced activity of K-dwarfs and the pileup of G-dwarfs older than a few Gyr are stellar-structure- and MB-dependent, and weakly dependent on core-envelope coupling effects; (3) our empirical expression of the core-envelope convergence time-scale $\tau_{\text{converge}}(M_*, P_{\text{spin}})$ between a few 10 to 100 Myr is strongly dependent on stellar structure and weakly dependent on MB strength and shear, where fast and massive rotators achieve corotation earlier; (4) our estimates of the surface magnetic fields are in general agreement with observations and our wind mass loss evolution explains the weak winds from the solar analog π^1 UMa; (5) the massive young Sun theory as a solution to the faint young Sun problem, which states that the early Sun was sufficiently more massive to maintain liquid water on Earth when the Sun's luminosity would have been about 30 percent lower, can likely be ruled out because the maximum mass lost by winds from our Sun with our model is about $0.001M_{\odot}$, an order of magnitude smaller than required to solve the problem with this theory.

Key words: stars: late-type – stars: low-mass – Sun: evolution – stars: pre-main-sequence – stars: protostars – stars: rotation.

1 INTRODUCTION

Magnetic braking (MB) is a mechanism by which stellar angular momentum is lost (Schatzman 1962). It operates in many single and binary stars and in many cases drives the long-term spin and orbital properties of a system. Accurate modelling of the MB torque and its evolution is especially crucial for the studies of low-mass stars and cataclysmic variables (Barnes 2003; Warner 2003).

Skumanich (1972) found that the equatorial rotation velocity of single G-dwarfs scales with their age t as $t^{-0.5}$. The subsequent torque scales with spin period P_{spin} as P_{spin}^{-3} (Verbunt & Zwaan 1981). However, it was soon evident that the MB torque has a weaker dependence on the rotational angular velocity Ω in rapidly spinning stars (Kawaler 1988; Wright et al. 2011). This has been incorporated in various MB models (Sills et al. 2000; Matt et al. 2015). Observations of isolated low-mass stars in open clusters (OCs) of known ages also revealed a bimodality in their rotation rates: the same OC contains a population of fast as well as slow rotators (Barnes 2003). Efforts have been made to explain this with mechanisms such as

stochastic changes in the MB torque (Brown 2014) or multipolar effects in the stellar magnetic fields (Garraffo et al. 2018).

Studying partly convective dwarfs (PCDs, $0.35 \lesssim M_*/M_{\odot} \lesssim 1.3$) poses an additional problem. While the evolution of P_{spin} of fully convective M-dwarfs (FCMDs, $M_* \lesssim 0.35 M_{\odot}$) can be well modelled assuming the whole star rotates as a solid body (SB), modelling PCDs as SBs is inconsistent with observations (Denissenkov et al. 2010). This is because PCDs possess a radiative core and a convective envelope. The radiative interior is not as efficient as the convective envelope at transporting angular momentum so the interior of the star can decouple, breaking down the SB rotation for such stars. So, modelling PCDs requires a mechanism for the transport of internal angular momentum within the star. This has been done in detailed stellar evolution codes that incorporate shellular rotation (Zahn 1992) in a star with angular momentum transport via the Tayler-Spruit dynamo (Spruit 2002; Eggenberger et al. 2022) by Denissenkov & Pinsonneault (2007) and Denissenkov et al. (2010) and with a simpler two-zone model by MacGregor & Brenner (1991), who used characteristic core-envelope coupling time-scales (Denissenkov et al. 2010). However, both of these approaches depend on two uncertain and interrelated mechanisms, MB and internal angular momentum transport (in the form of the coupling time-scale in the latter approach). The problem is two-fold: not only do we require the

★ E-mail: as3158@cam.ac.uk

† E-mail: cat@ast.cam.ac.uk

surface rotation rates of our models to agree with robust observations (Godoy-Rivera et al. 2021; Pass et al. 2022), but we also require that the core and the envelope corotate within Gyr time-scales as shown by the internal rotation of the Sun (Thompson et al. 2003) and suggested by asteroseismic data for stars with $M_* \gtrsim 0.8M_\odot$ (Bétrisey et al. 2023). Several aspects of the spin evolution of PCDs have been addressed using a semi-empirical approach (Sadeghi Ardestani et al. 2017) or a holistic framework combining stellar activity and spindown (Blackman & Owen 2016). In a series of papers, we have illustrated that robust modelling of MB can help explain the observational properties of many single- and binary-star systems (Sarkar & Tout 2022 for cataclysmic variables, Sarkar et al. 2023a and Sarkar et al. 2023b for AM Canum Venaticorum stars, and Sarkar et al. 2023c for FCMDs). Recently Sarkar et al. (2023c, hereinafter SYT I) used an $\alpha - \Omega$ dynamo mechanism of MB to explain the spin evolution of FCMDs. A modified version of this MB mechanism was used earlier to explain the observations of cataclysmic variables and AM Canum Venaticorum stars. In this paper, we extend our analysis to holistically model partly convective low-mass stars and address several theoretical and observational constraints on their evolution.

In Section 2 we provide the details of our model of MB and angular momentum transport. In Section 3 we study the behaviour of our model in PCDs of various masses and the dependence of the spin evolution of the core and the envelope on uncertain parameters in our MB and angular momentum transport mechanism. We present our results and discuss their implications in Section 4. We conclude in Section 5.

2 MAGNETIC BRAKING AND INTERNAL TRANSPORT OF ANGULAR MOMENTUM

A schematic diagram illustrating the core and envelope properties of PCDs in our model is shown in Fig. 1. In our model, MB in the star is caused by an $\alpha - \Omega$ dynamo operating in the convective zone. We model this with the formalism of Tout & Pringle (1992, hereinafter TP) for contracting pre-main sequence (PMS) stars. We use a two-zone model with a uniformly rotating radiative core and convective envelope (MacGregor & Brenner 1991) but employ a mechanism of shear according to Zangrilli et al. (1997).

2.1 The convective dynamo

The basic formulation of our $\alpha - \Omega$ dynamo in the convective envelope is the same as in SYT I, albeit with a few updates. We urge the reader to refer to this paper and only highlight here the changes made to the model for a partly convective envelope. Hereinafter the subscript env denotes the convective envelope (star) in a PCD (FCMD) while core denotes the radiative core (if any).

Like SYT I, we assume that the convective envelope rotates as a solid body and parametrize the differential rotation with an average across the envelope as $\Delta\Omega_{\text{env}} \approx R_{\text{env}}/R_* \Omega_{\text{env}}$ ¹. This definition ensures that $\Delta\Omega_{\text{env}} \rightarrow \Omega_{\text{env}}$ for FCMDs and that the smaller the thickness of the envelope, the lower its average differential rotation. This is the Ω term in our $\alpha - \Omega$ dynamo, which converts poloidal fields into toroidal fields. The dynamo is completed when the regeneration term or the α term in the $\alpha - \Omega$ dynamo converts toroidal fields into

poloidal fields. The equilibrium equations remain the same as used by SYT I:

$$\frac{dB_\phi}{dt} = \Delta\Omega_{\text{env}} B_p - \frac{B_\phi}{\tau_\phi} = 0 \quad (1)$$

and

$$\frac{dB_p}{dt} = \frac{\Gamma}{R_*} B_\phi - \frac{B_p}{\tau_p} = 0, \quad (2)$$

where B_ϕ is an average toroidal component of the magnetic field in the star, B_p is the poloidal component of the magnetic field, τ_ϕ and τ_p are the time-scales on which the poloidal and toroidal magnetic field components are destroyed and Γ is the dynamo regeneration term. Γ is defined similarly to Parker (1955) and Cowling (1981) so that

$$\Gamma \approx \tau_t \nu_t \omega_t = \gamma \nu_c, \quad (3)$$

where τ_t is the turbulent turnover time-scale, $\nu_t \approx v_c$ is the velocity of turbulent cells, ν_c is the convective velocity and $\omega_t \propto \Omega$ is the vorticity of the eddies parallel to v_c . We write γ similarly to equation (5) of SYT I (see also their section 2.1)

$$\gamma = f_1 \frac{M_*}{0.35M_\odot} \sqrt{\frac{R_*}{g}} \Omega_{\text{env}}, \quad (4)$$

where f_1 is a parameter of the order unity which we calibrate in Section 2.5. Here $M_*/0.35M_\odot$ is the mass that undergoes cyclonic turbulence, normalized to $0.35M_\odot$ which we take to be the maximum mass of a FCMD. We assume that turbulent instabilities turn over in the shortest time-scale possible. We take this to be the sound-crossing time over the stellar radius (Spruit 2002) and define $\tau_t \approx \sqrt{R_*/g}$, where g is the surface gravity.

2.2 Wind mass loss calculation

We extend the arguments of SYT I and assume that the energy input by differential rotation in the envelope is comparable to its rotational kinetic energy, but make careful modifications to take into account the fact that the star is only partly convective. The rate at which energy is fed into the shear in the convective zone is given by

$$L_w \approx \frac{\frac{1}{2} I_{\text{env}} \left(\frac{R_{\text{env}}}{R_*} \Omega_{\text{env}} \right)^2}{\tau_v}, \quad (5)$$

where I_{env} is the moment of inertia of the envelope and τ_v is the viscous-time scale given by

$$\tau_v = \frac{R_{\text{env}}^2}{\nu}, \quad (6)$$

where ν is the convective viscosity. SYT I assumed that an arbitrary value of 10 percent of the deposited energy escapes as winds, and the rest is radiated away. We also implement this factor here. However, the fraction of energy escaping in winds should change when a star transitions from a fully convective PMS star to a main-sequence (MS) star. Similarly, this fraction should be different for

¹ We note that R_{env} is the width of the envelope (and not the location of the base of the envelope). The location of the base of the convective envelope is given by $R_* - R_{\text{env}} = R_{\text{core}}$.

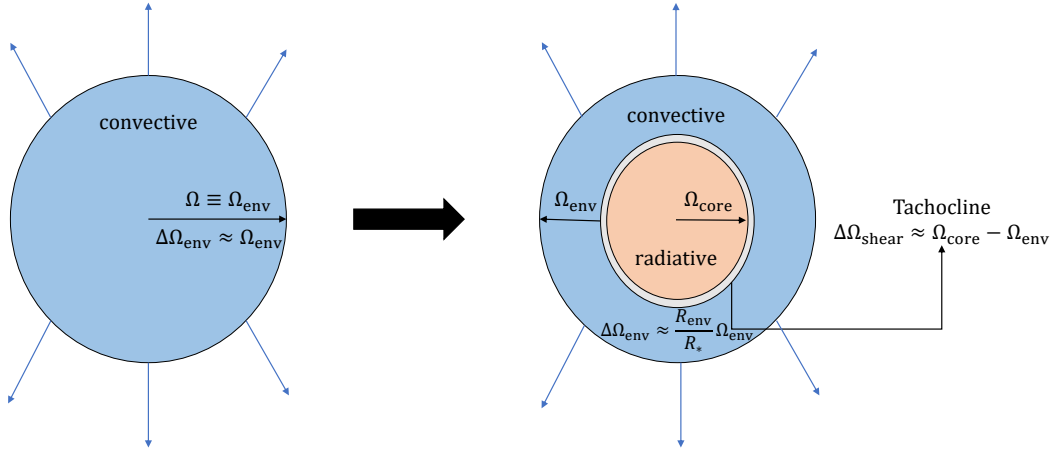


Figure 1. A schematic diagram of the various parameters with which we model the spin of the core and envelope of a fully convective pre-main-sequence star (left) that evolves to a partly convective main-sequence low-mass star (right). The blue lines emerging out of the surface of the star denote MB due to our $\alpha - \Omega$ dynamo mechanism (Section 2.1). The schematic on the left also describes the evolution of fully convective M-dwarfs.

stars of different masses. These effects are encapsulated by the coronal temperature T_{cor} . We argue that a larger fraction of the total shear luminosity is radiated away for a larger T_{cor} . [Johnstone & Güdel \(2015\)](#) have used X-ray emission data of low-mass stars to derive how T_{cor} scales with stellar mass and spin. They find that for MS stars $T_{\text{cor}} \propto M_*^{0.6}$ in the saturated regime and $T_{\text{cor}} \propto M_*^{-0.42} \Omega_*^{0.52}$ in the unsaturated regime. However, these relations do not encapsulate the behaviour of T_{cor} of contracting PMS stars. This is extremely difficult to estimate reliably so we introduce an additional reduction of $(M_{\text{env}}/M_*)^2 (M_*/M_\odot)^{-0.25}$ in the wind mass loss rate for partly convective stars. The term $(M_{\text{env}}/M_*)^2$ illustrates that the fraction of wind energy reduces drastically when the star transitions from its fully convective PMS phase to the partly convective MS phase. The term $(M_*/M_\odot)^{-0.25}$ illustrates that a larger fraction of the energy is radiated away in more massive stars. The exponents are ad hoc but yield realistic wind mass-loss rates for the Sun at its current age t_\odot . We write

$$0.1 \left(\frac{M_{\text{env}}}{M_*} \right)^2 \left(\frac{M_*}{M_\odot} \right)^{-0.25} L_w \approx \frac{GM_* \dot{M}_w}{R_*}, \quad (7)$$

where G is Newton's gravitational constant. We then obtain an expression for the wind mass-loss rate

$$\dot{M}_w = f_{\text{corot}} f_{\text{DZ}} \left(\frac{M_{\text{env}}}{M_*} \right)^2 \left(\frac{M_*}{M_\odot} \right)^{-0.25} \frac{I_{\text{env}}}{20} \frac{\Omega_{\text{env}}^2 \nu}{GR_* M_*}, \quad (8)$$

where f_{DZ} is a dimensionless quantity, less than 1, which measures the effect of a dead zone on the star's mass-loss rate. The calculation of dead zones stays identical to that for fully convective stars and has been explained in detail by [SYT I](#). The parameter f_{corot} is a dimensionless quantity that measures an enhancement in the winds (as well as a reduction in the Alfvén radius, described in Section 2.3). The expression for ν is the same as that of [SYT I](#):

$$\nu \approx \frac{1}{3} v_c l_c \min \left(\left(\frac{2\pi f_2}{\tau_c \Omega_{\text{env}}} \right)^p, 1 \right), \quad (9)$$

where

$$v_c \approx \left(\frac{L_* R_*}{\eta M_*} \right)^{1/3}. \quad (10)$$

Here L_* is the luminosity of the star, $\eta \approx 3R_{\text{env}}/l_c \approx 30$ is a constant ([Campbell & Papaloizou 1983](#)) and l_c is the mixing length. The factor $\min((2\pi f_2/\tau_c \Omega_{\text{env}})^p, 1)$ quantifies the curtailment in the convective viscosity for a rapidly rotating star (see section 2.2 of [SYT I](#) for details). The factor $f_2 \gtrsim 1$ is a free parameter that dictates the Ω_{env} at which ν is curtailed and $p \geq 0$ measures how strongly the convective viscosity is curtailed when $\Omega_{\text{env}} \tau_c > 2\pi f_2$ (p is calibrated in Section 2.5). Now \dot{M}_w becomes

$$\dot{M}_w = f_{\text{corot}} f_{\text{DZ}} \left(\frac{M_{\text{env}}}{M_*} \right)^2 \left(\frac{M_*}{M_\odot} \right)^{-0.25} \frac{I_{\text{env}}}{60} \frac{\Omega_{\text{env}}^2}{GR_* M_*} v_c l_c \min \left(\left(\frac{2\pi f_2}{\tau_c \Omega_{\text{env}}} \right)^p, 1 \right). \quad (11)$$

2.3 Alfvén radius, magnetic field, and angular momentum loss rate

The winds that emerge from the star are forced to corotate with it to the Alfvén radius, where the kinetic energy density in the wind equals the magnetic energy density and so

$$v_A^2 \approx \frac{B_p(R_A)^2}{4\pi\rho_A}, \quad (12)$$

where the subscript A denotes the Alfvén surface and B_p is the dipole component of the magnetic field. SYT I assumed that the wind density ρ_A at the Alfvén surface is

$$\rho_A = \frac{\dot{M}_w}{4\pi R_A^2 v_A}. \quad (13)$$

This is valid for a spherically symmetric wind. However, because of our implementation of the dead zones, not only does \dot{M}_w reduce, but there is also a non-spherical wind mass loss profile (see Garraffo et al. 2015 who show that magnetized winds are not distributed evenly at the stellar surface). This leads to a decrease in the surface area from which winds escape and consequently increases ρ_A . We measure this decrease in surface area by redefining ρ_A such that

$$\rho_A = \frac{\dot{M}_w}{f_{\text{non-sph}} 4\pi R_A^2 v_A}, \quad (14)$$

where $f_{\text{non-sph}}$ can be calculated if we know f_{DZ} . Mestel & Spruit (1987) defined $\sin^2\theta \equiv f_{\text{DZ}} = R_*/r_{\text{DZ}}$, where r_{DZ} is the equatorial radius of the dead zone. A larger r_{DZ} leads to a larger dead zone and, as a consequence, a smaller f_{DZ} . So the fractional surface of the wind-emitting region of the star can be calculated as

$$f_{\text{non-sph}} = \epsilon \int_0^{\sin^{-1}(\sqrt{f_{\text{DZ}}})} \sin\theta \, d\theta = \epsilon \left(1 - \sqrt{\frac{r_{\text{DZ}} - R_*}{R_*}} \right), \quad (15)$$

where $\epsilon \ll 1$. For a star with a spherically symmetric wind (without dead zones) $f_{\text{non-sph}} = 1$. However, the simulation results of Garraffo et al. (2015) show that winds are emitted only at certain latitudes where there are star-spots. This leads to a further mass-, radius- and likely spin-dependent reduction in the fraction of contributing surface area. This is extremely difficult to model so we simply incorporate it into ϵ by

$$\epsilon = 0.04 \left(\frac{M_\odot}{M_*} \right)^\delta. \quad (16)$$

Note that we introduce a new parameter δ that governs ϵ . This equation illustrates that, with increasing stellar mass, the wind-emitting regions on the stellar surface become more spotted and equation (14) deviates further from the spherically-symmetric wind assumption. We now assume that the magnetic field falls off as a dipole everywhere (although see Garraffo et al. 2015, 2016 for a discussion on multipolar contribution to the magnetic field) so that

$$B_p(R) = B_p(R_*) \left(\frac{R_*}{R} \right)^3. \quad (17)$$

Unlike SYT I we define the velocity at the Alfvén surface to be the escape velocity at the Alfvén radius R_A such that

$$v_A = \sqrt{\frac{2GM_*}{R_A}}. \quad (18)$$

Because of this slight change in defining v_A , R_A differs from equation (18) of SYT I:

$$R_A = f_{\text{non-sph}}^{-2/7} \frac{R_*^{12/7} (B_p(R_*))^{4/7}}{\dot{M}_w^{2/7} (2GM_*)^{1/7}}. \quad (19)$$

The calculations of TP and Zangrilli et al. (1997) were for stars whose corotation radius $R_\Omega \equiv (GM_*/\Omega^2)^{1/3}$ was larger than the Alfvén radius, so that the winds emitted from the photosphere were constantly decelerated. The calculations of SYT I did not take into account the scenario where $R_\Omega < R_A$ which is observed in many fast-spinning stars (Villarreal D’Angelo et al. 2018). Regős & Tout (1995) considered the case where $R_\Omega < R_A$ in which case winds are accelerated centrifugally beyond R_Ω and can have velocities greater than the escape velocity at the Alfvén radius. This would lead to an enhancement in the wind mass loss and a reduction in R_A . We model the effect as follows. When $R_A > R_\Omega$, owing to centrifugal acceleration the kinetic energy of the winds increases. This leads to an enhancement in the winds which we model with $\dot{M}_w \propto v^2 \propto (R_A/R_\Omega)$. This is taken into account in the factor f_{corot} in equation (11). We assume that the wind velocity at the Alfvén surface increases leading to a decrease in R_A such that it cancels the increase in \dot{M}_w and $\dot{J}_w \propto \dot{M}_w R_A^2$ remains unchanged. In order to ensure this, we add a factor $f_{\text{corot}}^{-3/14}$ to equation (19) which becomes

$$R_A = f_{\text{corot}}^{-3/14} f_{\text{non-sph}}^{-2/7} \frac{R_*^{12/7} (B_p(R_*))^{4/7}}{\dot{M}_w^{2/7} (2GM_*)^{1/7}}, \quad (20)$$

where

$$f_{\text{corot}} = \max \left(\left(\frac{R_A}{R_\Omega} \right), 1 \right). \quad (21)$$

The dynamo mechanism leads to a surface poloidal field which is given by equation (4.10) of TP modified for a partly convective star:

$$B_p(R_*) = 10\gamma v_c \sqrt{4\pi\rho_{\text{env}}}, \quad (22)$$

where $\rho_{\text{env}} = M_{\text{env}}/(4/3\pi R_*^3 - 4/3\pi R_{\text{core}}^3)$ is the mean density of the convective envelope. Beyond the Alfvén radius, the winds escape freely, carrying away angular momentum. So we write the angular momentum loss by MB as

$$\dot{J}_w = -\dot{M}_w R_A^2 \Omega_{\text{env}}. \quad (23)$$

2.4 Core-envelope shear

We model the shear at the core-envelope boundary based on the arguments of Zangrilli et al. (1997, their section 4). We assume for simplicity that the radiative core spins as a solid body with Ω_{core} . Thus the differential rotation at the core-envelope boundary is

$$\Delta\Omega_{\text{shear}} = \Omega_{\text{core}} - \Omega_{\text{env}}. \quad (24)$$

When $\Delta\Omega_{\text{shear}} \neq 0$, any convective cell that overshoots from the envelope to the core experiences a toroidal field, which is a function of $\Delta\Omega_{\text{shear}}$, at the boundary. A consequence of this effect is a shear term that spins down the core if $\Delta\Omega_{\text{shear}} > 0$ and vice versa. In other words, differential rotation at the core-envelope boundary creates an angular momentum transport mechanism between the two regions.

Following the arguments of Zangrilli et al. (1997), the toroidal field generated at the boundary layer decays quickly beyond the thickness of the boundary layer H_B . This is because we assume that the differential rotation responsible for the strong toroidal field only persists in the boundary layer. So we define the decay time-scale for the toroidal field as

$$\tau_\phi = \frac{10H_B}{v_\phi}, \quad (25)$$

where $v_\phi = B_\phi / \sqrt{4\pi\rho_B}$. The factor of 10 arises because we assume that the field decays by magnetic buoyancy, which we assume operates about 10 times more slowly than the Alfvén-wave crossing time (see section 4 of TP for details). However, the poloidal field is generated throughout the convective layer because of the α -effect and only decays beyond R_{env} . So the decay time-scale for the poloidal field is

$$\tau_p = \frac{10R_{\text{env}}}{v_p}, \quad (26)$$

where $v_p = B_p / \sqrt{4\pi\rho_B}$. Now, using equations (1) and (2), we get

$$v_p = 10\gamma^{2/3} v_c^{2/3} \left(\frac{R_{\text{env}}}{R_*} \right)^{2/3} \Delta\Omega_{\text{shear}}^{1/3} H_B^{1/3} \quad (27)$$

and

$$v_\phi = 10\gamma^{1/3} v_c^{1/3} \left(\frac{R_{\text{env}}}{R_*} \right)^{1/3} \Delta\Omega_{\text{shear}}^{2/3} H_B^{2/3}. \quad (28)$$

The angular momentum transfer between the core and the envelope is given by

$$j_{\text{shear}} = \left(\frac{B_p B_\phi}{4\pi} \right) V_B = f_{\text{shear}} 100\gamma v_c \left(\frac{R_{\text{env}}}{R_*} \right) \Delta\Omega_{\text{shear}} H_B^2 R_{\text{core}}^2 4\pi\rho_B, \quad (29)$$

where $f_{\text{shear}} \leq 1$ is a free parameter that measures the efficiency of shear to transport angular momentum, $V_B = 4\pi H_B R_{\text{core}}^2$ is the volume of the boundary layer and $\rho_B = M_B/V_B$, where M_B is the mass of the boundary layer (also see equation 13 of Wickramasinghe et al. 2013). We define a simple empirical expression of H_B as

$$H_B \equiv 0.0645 R_{\text{env}}. \quad (30)$$

The factor 0.0645 gives $H_B \approx 0.02R_\odot$ at $t \approx 4.6$ Gyr for a $1M_\odot$ star. This is close to the size of the solar tachocline as estimated by Basu & Antia (2003). With equation (30) we can estimate the thickness of the boundary layer (tachocline) of a star of a given mass at all evolutionary times.

2.5 Calibration of free parameters and a summary of updates

The parameters f_1 , f_2 , p , δ , and f_{shear} must be estimated before we can use our model to evolve PCD spins. We keep f_2 , δ and f_{shear} as free parameters and fix f_1 and p as follows.

- f_1 : Using equation (4) in equation (22), we obtain f_1 as a function of t , B_p , M_* , R_* , L_* and P_{spin} . Using solar data from Table 1 and M_{env} and R_{env} at t_\odot using STARS, we obtain $f_1 \approx 0.115$.

Table 1. Solar data used in this work.

Symbol	Value
M_\odot	1.989×10^{33} g
R_\odot	6.96×10^{10} cm
L_\odot	3.85×10^{33} erg s $^{-1}$
P_\odot	26.09 d
t_\odot	4.6 Gyr
$\dot{M}_{w\odot}$	$2 \times 10^{-14} M_\odot$ yr $^{-1}$
$B_{p\odot}$	1 G
$R_{A\odot}$	10 to 20 R_\odot

Table 2. A table of parameters and a description of their estimates.

Parameter	Description
f_2 , equation (9)	Critical Rossby number
δ , equation (16)	Probes the behaviour of the wind-emitting surface
f_{shear} , equation (29)	Efficiency of shear

- p : This parameter measures how strongly convective viscosity is reduced for a fast-spinning star (when $\Omega_{\text{env}}\tau_c > 2\pi f_2$). We fixed $p = 4$ in SYT I (see their section 3.1) which gave $\dot{J}_w \propto \Omega$ in the saturated regime and $\dot{J}_w \propto \Omega^3$ in the unsaturated regime. Owing to the redefinition of R_A in equation (20), we now have

$$j \propto \begin{cases} \Omega_{\text{env}}^{3-\frac{3p}{7}}, & \text{when } 2\pi f_2/\tau_c \Omega_{\text{env}} \leq 1 \text{ (saturated),} \\ \Omega_{\text{env}}^3, & \text{otherwise (unsaturated).} \end{cases} \quad (31)$$

which gives us the desired proportionality when $p = 14/3$.

Our three free parameters are tabulated in Table 2 and we summarise the changes implemented in our MB modelling since the work of SYT I in Table 3.

3 MODELLING OF THE SPIN EVOLUTION

We can now model the spin evolution of any fully convective or partly convective star with a convective envelope and a radiative core if we know the time evolution of L_* , R_* , M_* , I_{core} , I_{env} , M_{core} , M_{env} , R_{core} , R_{env} and M_B . We use the Cambridge stellar evolution code STARS (Eggleton 1973; Pols et al. 1995) to obtain these parameters as a function of time at solar metallicity. We assume, similarly to SYT I, that the winds do not reduce the stellar mass significantly and so keep M_* constant with time. We also assume that the spin evolution of the star does not alter any of the parameters above and these parameters only change because of non-rotational stellar evolution.

The equations that govern the angular momentum evolution of the core J_{core} and the envelope J_{env} are two ordinary differential equations:

$$j_{\text{core}} = \begin{cases} -j_{\text{shear}} + \frac{2}{3} \dot{M}_{\text{core}} R_{\text{core}}^2 \Omega_{\text{env}}, & \text{if } \dot{M}_{\text{core}} > 0 \\ -j_{\text{shear}} + \frac{2}{3} \dot{M}_{\text{core}} R_{\text{core}}^2 \Omega_{\text{core}}, & \text{if } \dot{M}_{\text{core}} \leq 0 \end{cases} \quad (32)$$

and

Table 3. A summary of the differences in the magnetic braking implementation of SYT I and this work with the calibrated values of certain parameters.

Parameter	In SYT I	In this work	Description of change/calibration
Convective length l_c	$\frac{R_*}{10}$	$\frac{R_{\text{env}}}{10}$	Reduction for smaller convective envelopes
Shear in convective zone $\Delta\Omega_{\text{env}}$	$\Omega \equiv \Omega_{\text{env}}$	$\frac{R_{\text{env}}}{R_*} \Omega_{\text{env}}$	Reduction in shear for smaller convective envelopes
Wind mass loss \dot{M}_w	$f_{\text{DZ}} \frac{1}{600} \frac{R_*}{G} \Omega^2 v_c l_c \min\left(\left(\frac{2\pi f_2}{\tau_c \Omega}\right)^P, 1\right)$	Equation (11)	Reduction in τ_v , parametrization of wind escape fraction
Measure of viscosity curtailment p	4	$\frac{14}{3}$	Due to the redefinition of R_A
f_1 , equation (4)	Free parameter	0.115	Calibrated using $B_{\text{p}\odot}$ at t_\odot
Alfvén wind density ρ_A	$\frac{\dot{M}_w}{4\pi R_A^2 v_A}$	Equation (14)	Reduction in the surface area of wind emission
Wind velocity at Alfvén surface v_A	$\sqrt{2GM_*/R_*}$	Equation (18)	Escape velocity at Alfvén radius
Surface poloidal field $B_p(R_*)$	$10\gamma v_c \sqrt{4\pi\rho_*}$	Equation (22)	Mean density of the convective envelope
Alfvén radius R_A	$R_* \left(\frac{B_p(R_*)^2 R_*^2}{\dot{M}_w \sqrt{2GM_*/R_*}} \right)^{1/4}$	Equation (20)	A different definition of v_A

$$j_{\text{env}} = \begin{cases} j_w + j_{\text{shear}} - \frac{2}{3} \dot{M}_{\text{core}} R_{\text{core}}^2 \Omega_{\text{env}}, & \text{if } \dot{M}_{\text{core}} > 0 \\ j_w + j_{\text{shear}} - \frac{2}{3} \dot{M}_{\text{core}} R_{\text{core}}^2 \Omega_{\text{core}}, & \text{if } \dot{M}_{\text{core}} \leq 0 \end{cases} \quad (33)$$

Equation (32) illustrates that the angular momentum of the core is governed by shear (the first term) as well as the structural change of the star (the second term) when regions of the star change from being convective to being radiative, for instance, at the end of the PMS phase in F, G, K and (certain) M stars. We assume that there is no discontinuity in the Ω profile of the star at the tachocline so that the core boundary always spins with Ω_{env} . Equation (32) illustrates that the same phenomena plus magnetic braking govern the angular momentum evolution of the envelope. Now, under the assumption of solid-body rotation in the core and the envelope such that they rotate with an average Ω_{core} and Ω_{env} throughout, we obtain

$$\dot{\Omega}_{\text{core}} = \begin{cases} \frac{-j_{\text{shear}} + \frac{2}{3} \dot{M}_{\text{core}} R_{\text{core}}^2 \Omega_{\text{env}} - \dot{I}_{\text{core}} \Omega_{\text{core}}}{I_{\text{core}}}, & \text{if } \dot{M}_{\text{core}} > 0 \\ \frac{-j_{\text{shear}} + \frac{2}{3} \dot{M}_{\text{core}} R_{\text{core}}^2 \Omega_{\text{core}} - \dot{I}_{\text{core}} \Omega_{\text{core}}}{I_{\text{core}}}, & \text{if } \dot{M}_{\text{core}} \leq 0 \end{cases} \quad (34)$$

and

$$\dot{\Omega}_{\text{env}} = \begin{cases} \frac{j_w + j_{\text{shear}} - \frac{2}{3} \dot{M}_{\text{core}} R_{\text{core}}^2 \Omega_{\text{env}} - \dot{I}_{\text{env}} \Omega_{\text{env}}}{I_{\text{env}}}, & \text{if } \dot{M}_{\text{core}} > 0 \\ \frac{j_w + j_{\text{shear}} - \frac{2}{3} \dot{M}_{\text{core}} R_{\text{core}}^2 \Omega_{\text{core}} - \dot{I}_{\text{env}} \Omega_{\text{env}}}{I_{\text{env}}}, & \text{if } \dot{M}_{\text{core}} \leq 0. \end{cases} \quad (35)$$

We note that the core can indeed have a radial dependence on Ω (Bétrisey et al. 2023; Eggenberger et al. 2019). This is encapsulated in our simple treatment of spins as averages such that $\Omega_{\text{core}} > \Omega_{\text{env}}$ is equivalent to the possibility of a larger Ω at the deep interior of a star.

3.1 Spin evolution of a $0.5M_\odot$ and a $1.0M_\odot$ star

We analyse the spin evolution of the core and envelope of a $0.5M_\odot$ and a $1.0M_\odot$ star in Fig. 2. These represent two qualitatively different PCD stars: the $0.5M_\odot$ star always has $I_{\text{env}} > I_{\text{core}}$ while in the $1.0M_\odot$ star $I_{\text{core}} > I_{\text{env}}$ after the PMS phase.

We assume that the stars do not undergo any spin evolution before the disc-locking time τ_{dl} (Rebull et al. 2004). After τ_{dl} , the $0.5M_\odot$ star is still fully convective. Until about 10 Myr $I_{\text{core}} \approx 0$ and I_{env} stays fairly constant. Beyond this, the radiative core emerges so I_{env} begins to decrease and the envelope loses angular momentum to the core (the last term in equations 32 and 33). The core gains angular momentum from the envelope and I_{core} increases. At the same time, the shear term (equation 29) operates on the core to slow its spin while spinning up the envelope. Overall, the star spins up because of the contraction of the PMS star. This remains the case until about the magenta line at 100 Myr, beyond which the core and the envelope attain an almost constant I . From then onwards the spin behaviour of the core and the envelope can be understood as follows. When I_{core} and I_{env} are relatively constant, we can write

$$\dot{\Omega}_{\text{core}} = \frac{-j_{\text{shear}}}{I_{\text{core}}} \quad (36)$$

and

$$\dot{\Omega}_{\text{env}} = \frac{j_w + j_{\text{shear}}}{I_{\text{env}}}. \quad (37)$$

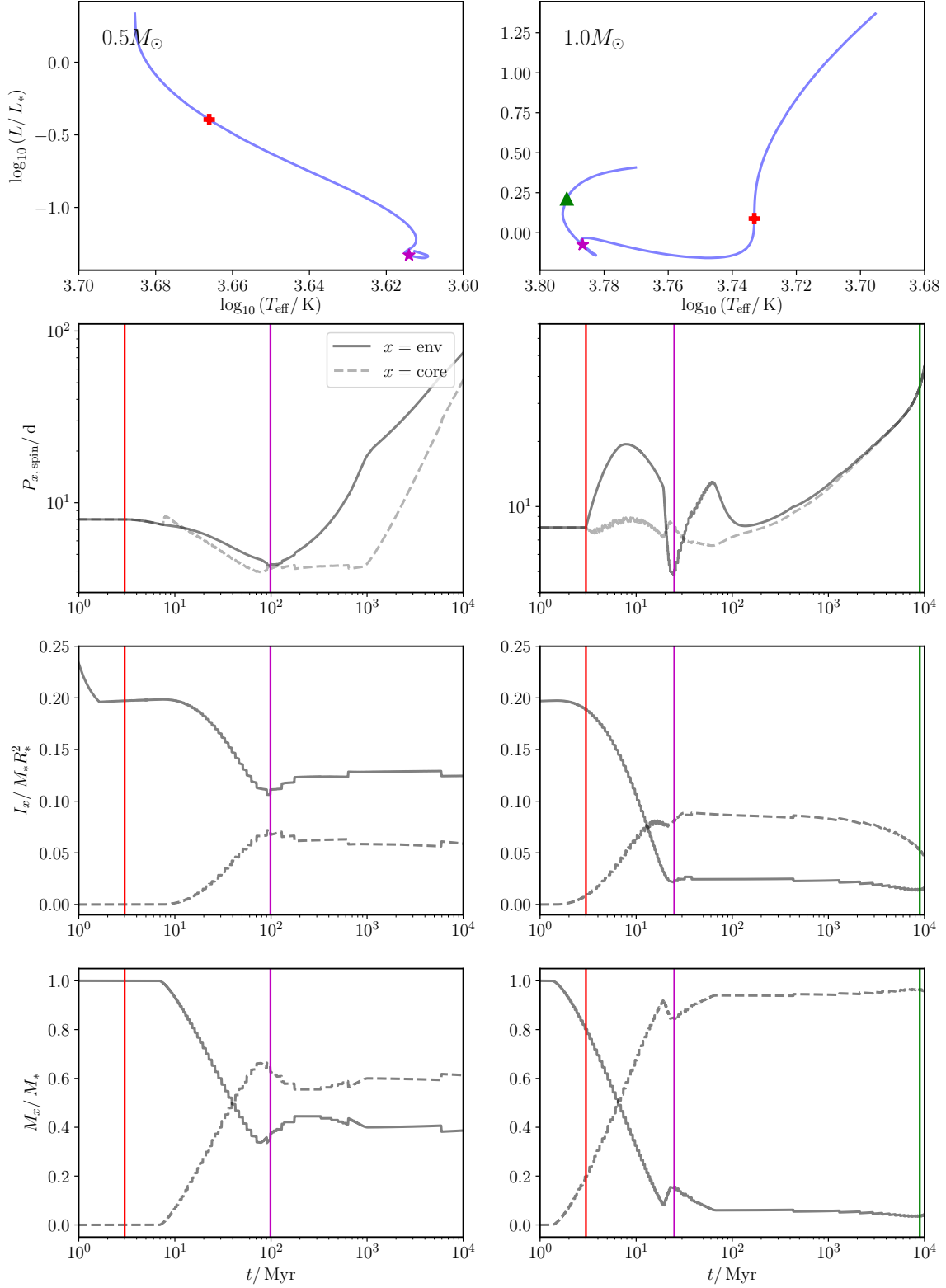


Figure 2. The evolution of the core and the envelope spin P_{spin} , moment of inertia I and masses with time for a $0.5M_{\odot}$ and $1.0M_{\odot}$ star with $P_{\text{spin, initial}} = 8$ d and $\tau_{\text{dl}} = 3$ Myr. The free parameters have been set as $f_2 = 1.5$, $f_{\text{shear}} = 0.1$ and $\delta = 1$. The red pluses (and the vertical lines of the same colour) denote the end of the disc-locking time. The magenta stars denote the minimum $P_{\text{env,spin}}$ and the green triangles the terminal age main sequence. The shaded region in the $P_{\text{spin}} - t$ plot denotes the region where $P_{\text{spin}} \leq P_{\text{crit}} \equiv \tau_c/f_2$.

The spin-down of the core is slower than the spin-down of the envelope when $-\dot{\Omega}_{\text{core}} < -\dot{\Omega}_{\text{env}}$ so when $\dot{\Omega}_{\text{core}} > \dot{\Omega}_{\text{env}}$. Note that $\dot{J}_w < 0$ and for spin-down $\dot{\Omega}_s < 0$. So using equations (36-37) we obtain

$$\text{If } \frac{-\dot{J}_w}{\dot{J}_{\text{shear}}} \begin{cases} > \frac{I_{\text{env}} + I_{\text{core}}}{I_{\text{core}}} \text{ then } \dot{\Omega}_{\text{core}} > \dot{\Omega}_{\text{env}} \text{ (core spins down slower),} \\ \leq \frac{I_{\text{env}} + I_{\text{core}}}{I_{\text{core}}} \text{ then } \dot{\Omega}_{\text{core}} \leq \dot{\Omega}_{\text{env}} \text{ (core spins down faster).} \end{cases} \quad (38)$$

The LHS of this equation is always positive for a more rapidly spinning core. For the $0.5M_{\odot}$ star, the core does not change in its spin before about 1 Gyr. This is because \dot{J}_{shear} is too weak to spin down the core and MB is strong so the first inequality in equation (38) holds. On the other hand, the envelope spins down rapidly by MB. Beyond about 1 Gyr, I_{core} decreases slightly allowing \dot{J}_{shear} to slow the core down more rapidly. The envelope's spin-down rate is reduced because now it is spun down by MB but spun up by shear (the second case in equation 38). However, the core and the envelope do not achieve corotation within the Galactic Age. This depends on the free parameters as illustrated in Section 3.2.

For the $1M_{\odot}$ star, the PMS phase has ended by τ_{dl} but the star is still dominantly convective. Owing to its strong wind mass loss (equation 11), the envelope experiences a very strong MB spin down which dominates over its contraction-driven spin up. Spin-up dominates from about 10 Myr till about 20 Myr when I_{env} is at its minimum. At the same time, I_{core} increases and the core also gains angular momentum from the envelope which keeps it spinning faster than the envelope. Interestingly, we see that from about 20 to 30 Myr, the core is spinning slower than the envelope. This is a stellar-structure-dependent effect and is due to the very rapid spin-up of the envelope when I_{env} is at its minimum. Beyond this, the envelope quickly spins down. At 50 Myr, the envelope and the core are slowly brought into near corotation by shear. The equality in the second case of equation (38) illustrates the behaviour of the star when the spin-down rates of the core and the envelope are the same. For the $1M_{\odot}$ star, beyond 30 Myr $(I_{\text{env}} + I_{\text{core}})/I_{\text{core}} \approx 1$ because of a small I_{env} . So shear and MB have similar strengths but MB is always stronger. In other words, the spinning-down envelope drags the core along with it. Because $(I_{\text{env}} + I_{\text{core}})/I_{\text{core}} > 1$, this ensures that a structurally constant star always spins down.

3.2 Dependence on free parameters

We now analyse the dependence of the spin-evolution trajectories on the free parameters in our model, f_{shear} , f_2 and δ , which govern the strength of shear in the boundary layer, the transition of the MB torque from the saturated to the unsaturated regime and the fraction of the wind-emitting surface of the star (see section 3 of SYT I for a detailed discussion of f_2).

3.2.1 Shear uncertainty

We first keep the MB-affecting terms f_2 and δ fixed while varying f_{shear} (Fig. 3). We see that a larger f_{shear} corresponds to a stronger angular momentum transfer mechanism by shear, that leads to the core and the envelope attaining corotation slightly earlier in the $1.0M_{\odot}$ star. For the $0.5M_{\odot}$ star, a stronger shear leads to a lower degree of differential rotation between the core and the envelope after a Gyr, with $\Delta\Omega_{\text{shear}} \approx 0$ by 10 Gyr when $f_{\text{shear}} = 0.3$ for both initial P_{spin} s.

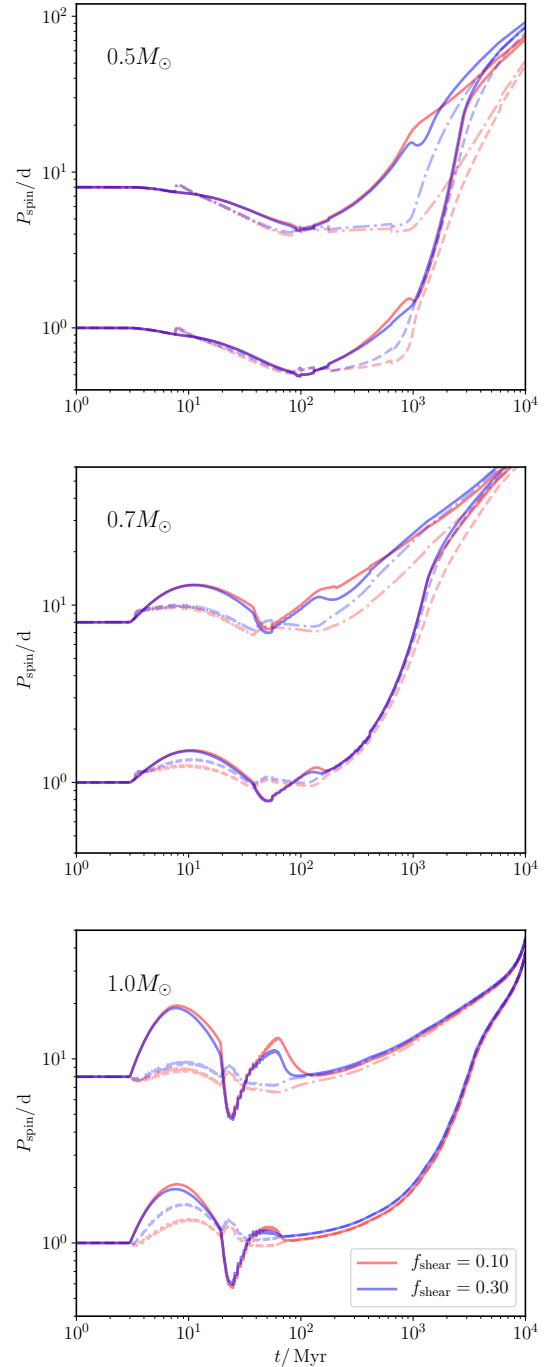


Figure 3. The evolution of the core (dashed for the fast rotators, dash-dotted for the slow rotators) and the envelope (solid) spin P_{spin} for $0.5M_{\odot}$, $0.7M_{\odot}$ and $1.0M_{\odot}$ stars with $P_{\text{spin, initial}}/d \in \{1, 8\}$ and $\tau_{\text{dl}} = 3$ Myr for different f_{shear} . The other free parameters have been set to $f_2 = 1.5$ and $\delta = 1$. The shaded region in the respective plots denotes the region where $P_{\text{spin}} \leq P_{\text{crit}} \equiv \tau_c/f_2$.

Changing the efficiency of shear leads to slight changes in the surface spin trajectory of only the slow-rotating $0.5M_{\odot}$ star, and only after a Gyr, while the $1.0M_{\odot}$ trajectories remain almost identical to each other. The effect is intermediate in the $0.7M_{\odot}$ star. In other words, our spin trajectories, particularly surface spins, are robust to changes in the efficiency of angular momentum exchange by shear.

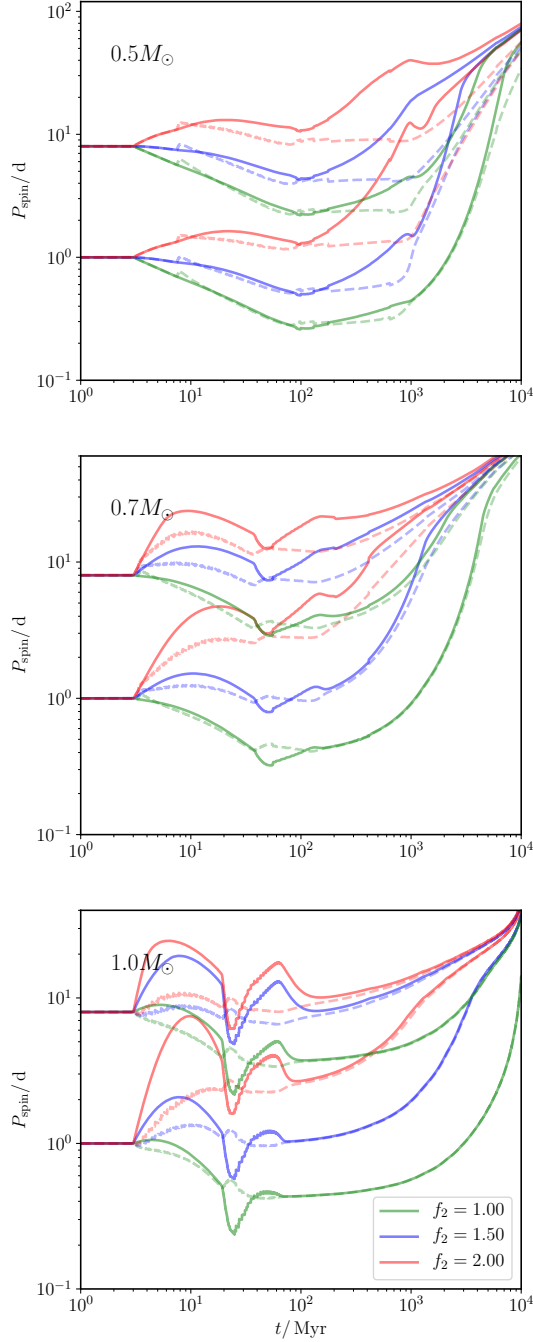


Figure 4. The evolution of the core (dashed) and the envelope (solid) spin P_{spin} for $0.5M_{\odot}$, $0.7M_{\odot}$ and $1.0M_{\odot}$ stars with $P_{\text{spin, initial}}/d \in \{1, 8\}$ and $\tau_{\text{dl}} = 3$ Myr for different values of f_2 . The other free parameters have been set to $f_{\text{shear}} = 0.1$ and $\delta = 1$. The shaded regions of different colours denote $P_{\text{spin}} \leq P_{\text{crit}} \equiv \tau_c/f_2$, where the colours of the shades denote the choice of f_2 . Each f_2 model should only be compared to its corresponding P_{crit} .

3.2.2 Magnetic braking uncertainty

We illustrate the effect of altering the MB strength on the spin trajectories by first changing f_2 while keeping δ fixed (Fig. 4). Changing f_2 leads to a change in $P_{\text{crit}} = \tau_c/f_2$, below which the MB torque is saturated ($\dot{J} \propto \Omega$) and above which it is unsaturated ($\dot{J} \propto \Omega^3$). Lower f_2 leads to a larger P_{crit} and also a weaker MB strength in the unsaturated regime ($\dot{J} \propto f_2^2$). In Fig. 4 the trajectories with $f_2 = 1$

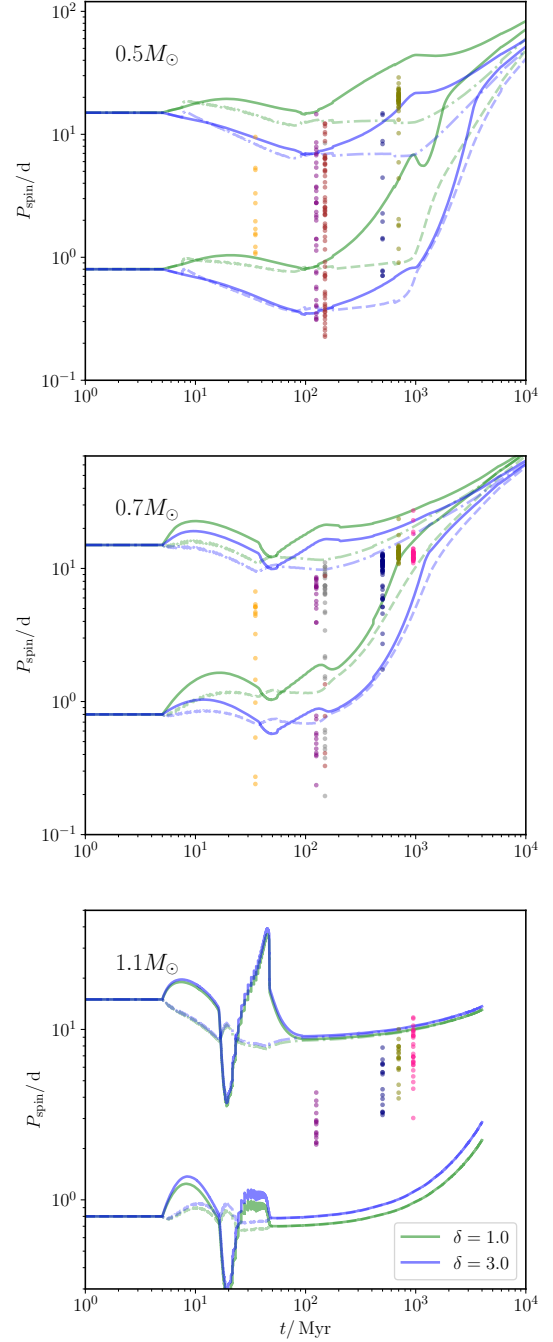


Figure 5. The evolution of the core spin (dashed for the fast rotators and dash-dotted for the slow rotators) and the envelope spin (solid) P_{spin} for $0.5M_{\odot}$, $0.7M_{\odot}$ and $1.1M_{\odot}$ stars with $P_{\text{spin, initial}}/d \in \{1, 8\}$ and $\tau_{\text{dl}} = 5$ Myr for various δ . The other free parameters are set to $f_{\text{shear}} = 0.1$ and $f_2 = 2$. The vertical arrays of dots denote observations of spins of stars in OCs of known ages by [Godoy-Rivera et al. \(2021\)](#). NGC2547 (35 Myr old), Pleiades (125 Myr old), M50 (150 Myr old), NGC2516 (150 Myr old), M37 (500 Myr old), Praesepe (700 Myr old) and NGC6811 (950 Myr old) are shown as vertical arrays of dots. The observations have been allocated to a subplot if their mass M_* lies in $[M_{\text{PCD}} - 0.05, M_{\text{PCD}} + 0.05] M_{\odot}$, where M_{PCD} is the mass considered in a subplot.

for each star undergo an initial spin-up because the MB torque is too weak to counter the contraction-driven spin-up. The trajectory with $f_2 = 2$ leads to a very strong torque even in the saturated regime. This dominates over contraction until about 20 Myr for $0.5M_\odot$ and about 5 Myr for $1.0M_\odot$. For a larger f_2 , the combined effect of a lower P_{crit} and a stronger torque in the saturated regime lead to the trajectory attaining a larger $P_{\text{env,spin}}$ at all times. A smaller f_2 leads to a shorter time to reach core-envelope corotation in both the stars. This can be understood with equation (38). The core can catch up with the envelope if it spins down more slowly. This is easier because a lower f_2 leads to a lower MB torque causing $-\dot{J}_w/\dot{J}_{\text{shear}}$ to be smaller. As expected, we also see that the spin trajectories depend on the magnetic braking strength. Our MB strength depends on two uncertain free parameters, f_2 and δ . Their effect on the MB torque can be illustrated as

$$-\dot{J}_w \propto \begin{cases} f_2^2 \epsilon^{-\frac{4}{7}}, & \text{if } (2\pi f_2 / \tau_c \Omega_{\text{env}}) \leq 1 \\ \epsilon^{-\frac{4}{7}}, & \text{otherwise,} \end{cases} \quad (39)$$

which simplifies to

$$-\dot{J}_w \propto \begin{cases} f_2^2 \left(\frac{M_*}{M_\odot}\right)^{\frac{4}{7}\delta}, & \text{if } (2\pi f_2 / \tau_c \Omega_{\text{env}}) \leq 1 \\ \left(\frac{M_*}{M_\odot}\right)^{\frac{4}{7}\delta}, & \text{otherwise.} \end{cases} \quad (40)$$

Changing f_2 affects the MB strength in the saturated regime while δ affects it at all times. Owing to our definition of equation (16), a larger δ leads to a lower MB torque for $M_* < 1M_\odot$ and vice versa. This is illustrated in Fig. 5, where we keep f_2 fixed and vary δ . The vertical arrays of dots are observations of open clusters of known ages from Godoy-Rivera et al. (2021).

Figs 4 and 5 show that, although the envelope spins are affected by MB, the core-envelope behaviour remains qualitatively the same for the $0.5M_\odot$ and $0.7M_\odot$ stars, and the $1.0M_\odot$ and $1.1M_\odot$ stars achieve near corotation at almost the same time for all f_2 and δ . This implies that the core-envelope behaviour is robust to changes in the efficiency of shear and magnetic braking strength. We also see that it strongly depends on the structural properties of the star and weakly depends on the initial spin. This has strong effects on the core-envelope convergence time-scale that we find in Section 4.2.

4 RESULTS AND DISCUSSION

We present the results of our model to address theoretical and observational constraints on the evolution of low-mass solar-like stars.

4.1 Surface rotation

In Fig. 6 we plot the spin-evolution with time of the core and the envelope of PCDs with masses between $0.4M_\odot$ and $1.1M_\odot$ for different initial P_{spin} and τ_{dl} . The vertical arrays of dots are observations of OC spins from Godoy-Rivera et al. (2021) and triangles of various colours denote the spins and inferred ages from Metcalfe et al. (2022, 2023). For the $0.4M_\odot$ star, the core abruptly vanishes after 1.5 Gyr. This is the case for stars with mass $0.3M_\odot \lesssim M_* \lesssim 0.4M_\odot$, which briefly develop a radiative core before it disappears. Such a core exists for only a few Myr in $0.3M_\odot$ stars while it is about a

Gyr in $0.4M_\odot$ stars. At higher masses, the mass of the radiative core becomes larger and persists permanently. We do not show the spin evolution of more massive PCDs because it does not change considerably beyond their PMS contraction phase. This is due to a very weak MB torque operating in such stars (in our model the MB strength is strongly proportional to M_*).

4.1.1 M-dwarfs

Our partly convective M-dwarf evolution tracks along with those for fully convective M-dwarfs in Fig. A1 show that the most massive fully convective M-dwarfs ($M_* \approx 0.35M_\odot$) are always spinning more slowly than their less massive counterparts ($M_* \lesssim 0.3M_\odot$) as well as more massive but partly convective M-dwarfs ($0.4M_\odot \lesssim M_* \lesssim 0.5M_\odot$). They also spin down more within the Galactic Age than partly convective M-dwarfs (Lu et al. 2023) and less massive FCMDs (Jao et al. 2023). In our model this is due to the MB torque being a function of M_* and M_{env}/M_* such that it attains a maximum at $0.35M_\odot$ which is the FCMD-PCD boundary.

4.1.2 K-dwarfs

K-dwarfs ($0.55M_\odot \lesssim M_* \lesssim 0.9M_\odot$) and the early M-dwarf of $0.5M_\odot$ show an interesting feature. It can be seen that the slow-rotating stars (initial $P_{\text{spin}} = 10$ d) show a change in their spin-down behaviour by either temporarily halting spin-down or slightly spinning up for P_{spin} between 10 and 20 d. For the $0.5M_\odot$ star, this happens between about 700 Myr to about 1.5 Gyr. This can be understood in Fig. 2. At around 1 Gyr, I_{core} decreases slightly, and so shear drives the spindown of the core more effectively. The strong angular momentum loss from the core feeds into the envelope, causing it to briefly spin up, thus generating a kink in P_{spin} at the surface. This effect is more prominent for larger values of f_{shear} (also see the $0.5M_\odot$ subplot in Fig. 3). The $0.6M_\odot$ star shows the same from about 300 Myr to 500 Myr, although the effect is weaker. The extent of spin-up depends on the MB strength but its duration seems to be independent of it (see Figs 4 and 5). The fast rotators (initial $P_{\text{spin}} = 1$ d) also show a change in their spin-down rates at the same time for a given PCD. The stalling effect is not visible in stars more massive than about $0.8M_\odot$ because the core and the envelope converge in their spins quite early on. This fits with observations that show that K-dwarfs experience a mass-dependent epoch of stalled spin-down and that the duration of stalling is longer for less-massive stars (Curtis et al. 2019). Curtis et al. (2020) and Spada & Lanzafame (2020) stated that an internal redistribution of angular momentum, owing to core-envelope coupling, can explain this behaviour. However, our models show that simply altering the internal angular momentum transfer efficiency has a very weak effect on the spin tracks of PCDs (Fig. 3). On the other hand, even decoupled tracks in Figs 4 and 5 show this stalling at the same age for a given star, albeit the P_{spin} at which it occurs is MB-dependent. This suggests that the stalling of P_{spin} in slow rotators is likely a MB-dependent and definitely a stellar-structure-dependent phenomenon (see the P_{spin} and I behaviour in Fig. 2).

4.1.3 G-dwarfs

We see that there is a weakening in the spin-down of both the slow- and the fast-rotators of the $1.0M_\odot$ and the $1.1M_\odot$ stars owing to a very weak MB torque acting on the envelope. This fits with the predictions of van Saders et al. (2019) who stated that a weak MB operates in

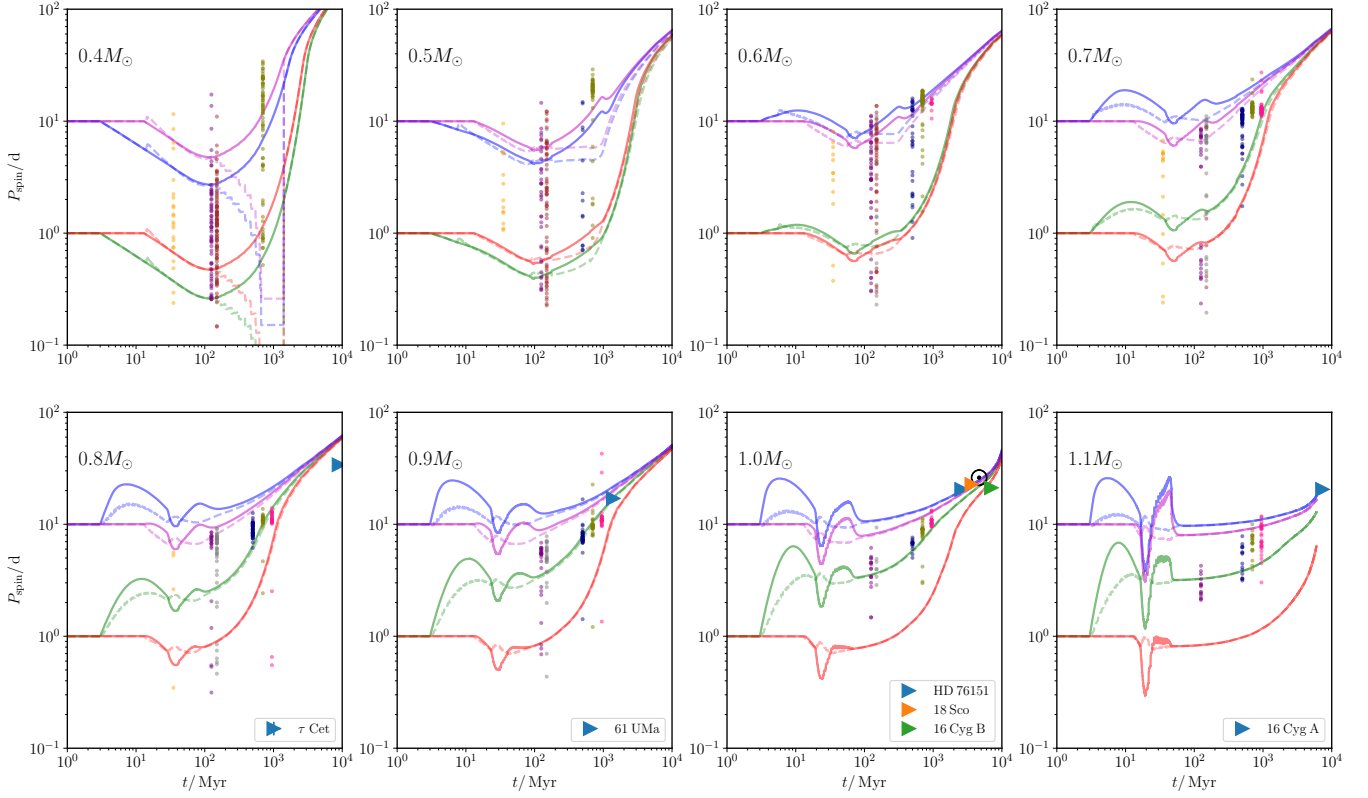


Figure 6. The core (dashed) and envelope (solid) spins of PCDs of various masses with $P_{\text{spin, initial}}/\text{d} \in \{1, 10\}$ and $\tau_{\text{dl}} \in \{3, 13\}$ Myr, $f_2 = 2$, $f_{\text{shear}} = 0.3$ and $\delta = 3$. The observations of OCs by [Godoy-Rivera et al. \(2021\)](#) are the same as in Fig. 5. The triangles of various colours are stars reported by [Metcalf et al. \(2022, 2023\)](#).

slowly rotating $M_* \gtrsim 1 M_\odot$ stars. This also explains the long-period pileup of such stars beyond 1 Gyr for several Gyr reported by [David et al. \(2022\)](#). For the fast-rotating $1 M_\odot$ star in Fig. 6 (green track), we see a rapid spin-down between about 100 Myr to 800 Myr when P_{spin} goes from a few to about 10 d while P_{spin} barely changes for the slow rotators. This transition region can explain the pileup at the short-period edge in the results of [David et al. \(2022\)](#) and is likely a dead-zone-dependent effect (fig. 4 of [SYT I](#)). However, this transition is not likely related to the core-envelope coupling mechanism in such stars because this transition is independent of the efficiency of shear (Fig. 3). Our tracks also show that such stars have corotating cores and envelopes at about 50 Myr. This is earlier than the observed pileups at a few Gyr. The strength of this rapid spin-down in fast rotators depends on MB (Figs 4 and 5). The age at which this transition takes place is the same for a given star. This suggests that it is also a stellar-structure-dependent phenomenon.

4.2 Internal rotation

The tracks in Fig. 6 show that the cores and envelopes achieve near corotation at a time that depends on their mass and spins. More massive stars achieve corotation earlier and rapidly spinning stars achieve corotation earlier than their slowly rotating counterparts of the same mass. The core-envelope coupling timescale τ_{couple} determines when the core and the envelope achieve corotation. It has been an important variable affecting the evolution of PCDs ([Denissenkov et al. 2010; Eggenberger et al. 2019; Spada & Lanzafame 2020; Bétrisey et al. 2023](#)). However, Figs 3, 4 and 5 show that τ_{couple} depends on the

efficiency of shear and the behaviour of the MB torque. So we define τ_{converge} as the age at which the core and the envelope achieve near corotation for fast rotators and tend to achieve corotation for slow rotators. This time weakly depends on uncertainties in MB and internal angular momentum redistribution efficiency². This time can be obtained from the abrupt drop in $\Delta\Omega_{\text{shear}}/\Omega_{\text{env}}$ after a local maximum in $\Delta\Omega_{\text{shear}}/\Omega_{\text{env}}$ (Fig. B1). It can also be seen in Fig. 6 where, for the $0.5 M_\odot$ star, the core and the envelope spins rapidly converge at about 1 Gyr. For the $1 M_\odot$ star this is at about 50 Myr. We find an empirical expression for τ_{converge} that depends on both M_* and P_{spin} . It is given by

$$\frac{\tau_{\text{converge}}}{\text{Myr}} \approx 22 \left(\frac{M_*}{M_\odot} \right)^{-5.42} + 17.82 \left(\frac{P_{\text{spin}}}{\text{d}} \right)^{0.59} \quad (41)$$

and is valid for $0.5 \lesssim M_*/M_\odot \lesssim 1.1$ and at all periods above breakup. Fig. 6 shows that for fast rotators $\tau_{\text{converge}} \approx \tau_{\text{couple}}$ while slow rotators have an ever-decreasing differential rotation beyond τ_{converge} . Interestingly, equation (41) is similar to the expression for τ_{couple} obtained by [Spada & Lanzafame \(2020\)](#) using the semi-empirical fitting of [Lanzafame & Spada \(2015\)](#), given by

² The slowly rotating $0.5 M_\odot$ and $0.7 M_\odot$ stars show a modest increase in their differential rotation as their core and envelope spins converge for certain choices of f_{shear} , f_2 and δ . This is alleviated if we choose a larger f_{shear} for a given MB strength or a lower MB strength for a given f_{shear} .

$$\frac{\tau_{\text{couple}}}{\text{Myr}} = 22 \left(\frac{M_*}{M_\odot} \right)^{-5.6}. \quad (42)$$

We can see that our expression (equation 41) tends to theirs (equation 42) as $P_{\text{spin}} \rightarrow 0$. That is, our expression reproduces their τ_{couple} limit for fast rotators.

4.3 Other observables

As illustrated by SYT I, a unique advantage of our model is that we obtain analytical estimates of the winds, the dipole component of the magnetic field (hereinafter just magnetic field) and the Alfvén radius at all times for a given star (equations 11, 22 and 20). These are plotted for a few PCDs in Fig. 7. The observationally inferred parameters are from Villarreal D’Angelo et al. (2018, pentagons) and Metcalfe et al. (2022, 2023, triangles). We see that, in general, our estimates are the best for $1M_\odot$ stars. This is possibly because we used solar data to calibrate our magnetic field (by setting $f_1 = 0.115$) and MB torque (equations 8 and 16). The estimates are not bad for $0.8M_\odot$ stars either. Interestingly, in the $\dot{M}_w - P_{\text{spin}}$ plane, $\dot{M}_w \approx \dot{M}_\odot$ at P_{spin} of about a few d for the $1M_\odot$ star evolved with initial $P_{\text{spin}} = 1$ d. This illustrates that winds as strong as that of the present-day Sun are possible in young solar-like stars. This can explain the observation reported by Wood et al. (2014) which found $\dot{M}_w = 0.5\dot{M}_\odot$ in a young, rapidly rotating solar analog star π^1 UMa.

We see that our estimates deviate for rapidly spinning configurations primarily for R_A which is, in general, overestimated by a factor of a few and \dot{M}_w that is underestimated by about an order of magnitude. This suggests that f_{corot} in equation (21) may be poorly defined. Overall, the surface magnetic field $B_p(R_*)$ estimates seem to be most robust (within a factor of a few) once the star begins to spin down smoothly. So we derive an empirical expression for this. Our expression for $B_p(R_*)$ (equation 22) is a simple function of stellar parameters M_* , L_* and R_* provided we know the spin and ρ_{env} . So, using equations (10, 4 and 22), we can write the magnetic field for any star B_{p*} as

$$\frac{B_p}{B_{p\odot}} = \left(\frac{L_*}{L_\odot} \right)^{1/3} \left(\frac{M_*}{M_\odot} \right)^{5/6} \left(\frac{R_*}{R_\odot} \right)^{7/6} \left(\frac{\Omega_*}{\Omega_\odot} \right) \left(\frac{\rho_{\text{env}}}{\rho_{\text{env}\odot}} \right)^{1/2}, \quad (43)$$

where we obtain $\rho_{\text{env}\odot} = 0.069 \text{ g cm}^{-3}$ from our STARS models. We fit $(\rho_{\text{env}}/\rho_{\text{env}\odot})^{0.5}$ as an empirical function of age t and M_* for $0.8M_\odot$, $0.9M_\odot$, $1.0M_\odot$ and $1.1M_\odot$ stars, obtaining

$$\left(\frac{\rho_{\text{env}}}{\rho_{\text{env}\odot}} \right)^{1/2} \approx -0.12 \left(\frac{t}{\text{Gyr}} \right) - 9.6 \left(\frac{M_*}{M_\odot} \right) + 11.6. \quad (44)$$

Using $L_* \propto M_*^{3.9}$ and $R_* \propto M_*^{0.8}$ for main-sequence stars, we obtain

$$\frac{B_p}{B_{p\odot}} \approx \left(\frac{M_*}{M_\odot} \right)^{3.07} \left(\frac{\Omega}{\Omega_\odot} \right) \left(-0.12 \left(\frac{t}{\text{Gyr}} \right) - 9.6 \left(\frac{M_*}{M_\odot} \right) + 11.6 \right). \quad (45)$$

This expression gives a simple estimate of the surface magnetic field within a factor of a few for solar-like main-sequence stars.

4.3.1 Is shear causing Praesepe K-dwarfs to be overactive?

It was recently reported by Cao et al. (2023) that slowly rotating ($P_{\text{spin}} \approx 10$ d) K-stars in the approximately 700 Myr-old Praesepe

OC are unusually overactive. The observation of enhanced activity in such stars, together with an apparent stalling of spin-down between the ages of Praesepe and the 950 Myr-old NGC 6811 (Curtis et al. 2019) was explained with core-envelope decoupling leading to to shear-enhanced activity in the convective envelope as well as a brief stalling of spin-down.

In Fig. 6, we see that all $0.5M_\odot$ stars achieve near corotation between the ages of Praesepe and NGC 6811 while the $0.7M_\odot$ stars do so much earlier at about 200 Myr. Beyond this age, the spinning-down envelope drags the core with increasing efficiency, thereby reducing differential rotation. The amount of differential rotation predicted by our model is negligible compared to that by Cao et al. (2023, see their fig. 2). However, we have discussed in Section 4.1.2 that the stalling of spin-down is a structure- and MB-dependent phenomenon and its duration and occurrence are sensitive to MB uncertainties. Fig. 7 shows that the $0.6M_\odot$ stars experience a sharp increase in their wind mass-loss rate \dot{M}_w at P_{spin} of about 10 d and that more massive stars do this at slower spins with the effect being less pronounced. This is due to the star transitioning from the saturated regime to the unsaturated regime (equation 11). Using \dot{M}_w as a proxy for stellar activity (Blackman & Owen 2016), we argue that this abrupt spike in wind mass loss in an otherwise monotonically decreasing magnetic field and Alfvén radius profile explains the unusual activity of such stars and that it is also a structure- and MB-dependent effect.

4.4 The Faint Young Sun paradox

When the Sun was formed about 4.6 Gyr ago as a zero-age main-sequence star, it had a luminosity of about $0.7L_\odot$. Based on this, calculations of the Earth’s ancient climate, under certain assumptions of its albedo and atmospheric composition, yield an average terrestrial temperature that is below water’s freezing point. However, there is ample geological evidence to suggest that water on the early Earth’s surface was liquid. This apparent contradiction is known as the Faint Young Sun paradox (Feulner 2012). Explanations for this problem include greenhouse gas solutions (Pavlov et al. 2000), cosmic rays (Shaviv 2003), albedo effects (Rosing et al. 2010) etc.

One of the solutions to this problem is the massive young sun hypothesis (Minton & Malhotra 2007). This theory suggests that when the Sun was born it was more massive than $1M_\odot$. As a result its luminosity was modestly higher and the Earth was closer to it. This kept Earth warm enough for liquid water. Over time, strong solar winds reduced the Sun’s mass to what we observe today while its luminosity increased. The reduction in stellar mass balanced the luminosity increase so as to have consistently warm enough temperatures on Earth to keep water liquid. Minton & Malhotra (2007) calculated the minimum mass loss that our Sun would have had to experience to resolve this paradox and found it to be about $0.026M_\odot$ and that the Sun needed to be more massive for about 2 Gyr after its formation. With our detailed mass loss model we can test this hypothesis. We calculate the mass-loss and spin evolution for a $1.0M_\odot$ star. Because our model does not alter the stellar properties due to mass loss, we cannot track the evolution of the mass loss in response to stellar properties. However, equation (11) shows that $\dot{M}_w \propto (M_{\text{env}}/M_*)^2 M_*^{-1.25}$, so the larger the stellar mass, the weaker the winds. Thus, the mass-loss profile of a $1.0M_\odot$ star represents the upper limit to the overall mass loss possible. We define Σ as the total mass lost before t_\odot as

$$\Sigma = \int_{\tau_{\text{dl}}}^{t_\odot} \dot{M}_w dt. \quad (46)$$

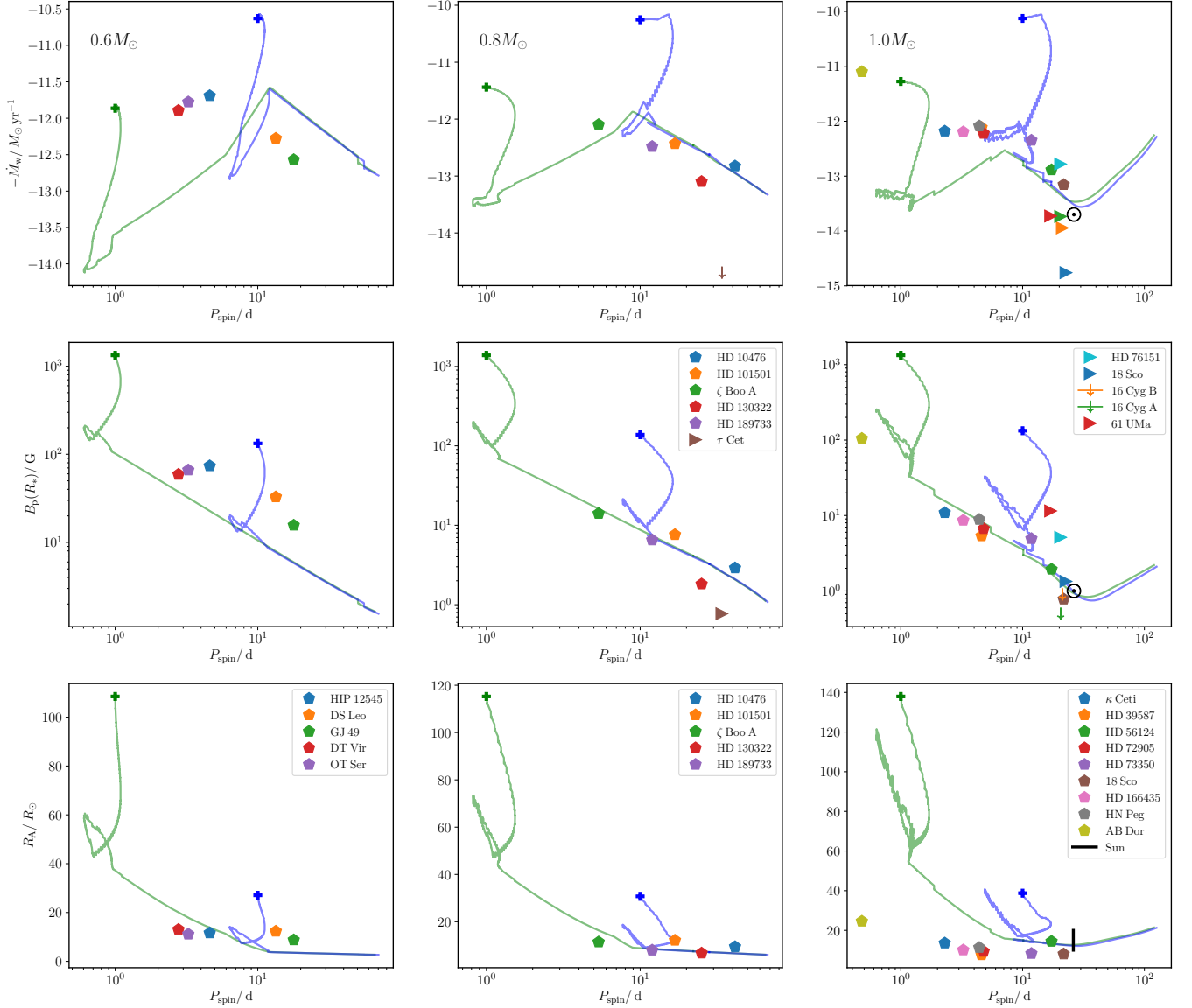


Figure 7. P_{spin} -dependent evolution of wind mass loss \dot{M}_w , dipole component of the poloidal magnetic field at the surface $B_p(R_*)$ and the Alfvén radius R_A for trajectories with $P_{\text{spin}} \in \{1, 10\} \text{ d}$, $\tau_{\text{dl}} = 5 \text{ Myr}$ and free parameters set to $f_2 = 2$, $f_{\text{shear}} = 0.3$, $\delta = 3$. The rough behaviour of the tracks at early times is because $\Delta\Omega_{\text{shear}}/\Omega_{\text{env}}$ is stiff for PCDs (also see Fig. B1). Though this can be removed numerically, there is little value in doing so because this effect lasts for only a few 10 Myr. The pluses of the same colour indicate the starting points of the trajectories. The observations are from Villarreal D’Angelo et al. (2018, pentagons) and Metcalfe et al. (2022, 2023, triangles). The minima in the \dot{M}_w -, $B_p(R_*)$ - and R_A - P_{spin} planes at about 30 d in the $1M_{\odot}$ star are due to its expansion after terminal-age main sequence at about 8 Gyr.

In order to maximize Σ , we set $\tau_{\text{dl}} = 3 \text{ Myr}$ and investigate initial spins equally spaced logarithmically between 1 and 30 d (Fig. 8). We see that \dot{M}_w drops to about an order of magnitude the current solar wind mass-loss rate between 20 Myr and 80 Myr and then converges to \dot{M}_{\odot} . However, Σ is always smaller than the $0.026M_{\odot}$ required to solve the faint young Sun problem. Even the most optimistic $\Sigma \approx 0.001M_{\odot} \ll 0.026M_{\odot}$ by about an order of magnitude. So, if our model is correct, we conclude that the massive young Sun theory is unlikely to be a viable solution to the faint young Sun problem as suggested by Minton & Malhotra (2007).

5 CONCLUSIONS

We have built a model to evolve the spins of the cores and the envelopes of partly convective dwarf stars (PCDs, $0.35 \leq M_*/M_{\odot} \leq 1.3$). This work extends that of Sarkar et al. (2023c) when we modelled the spin evolution of fully convective M-dwarf stars (FCMDs, $M_* \lesssim 0.35M_{\odot}$). We list the important components of our model.

- (i) The convective envelopes and the radiative cores of our PCDs rotate as solid bodies. The spin of the core is influenced by shear, which acts to transport angular momentum between the core and the envelope. The spin of the envelope is influenced by angular momentum loss by magnetic braking (MB) and shear.
- (ii) Our MB formalism is the same as that of Sarkar et al. (2023c)

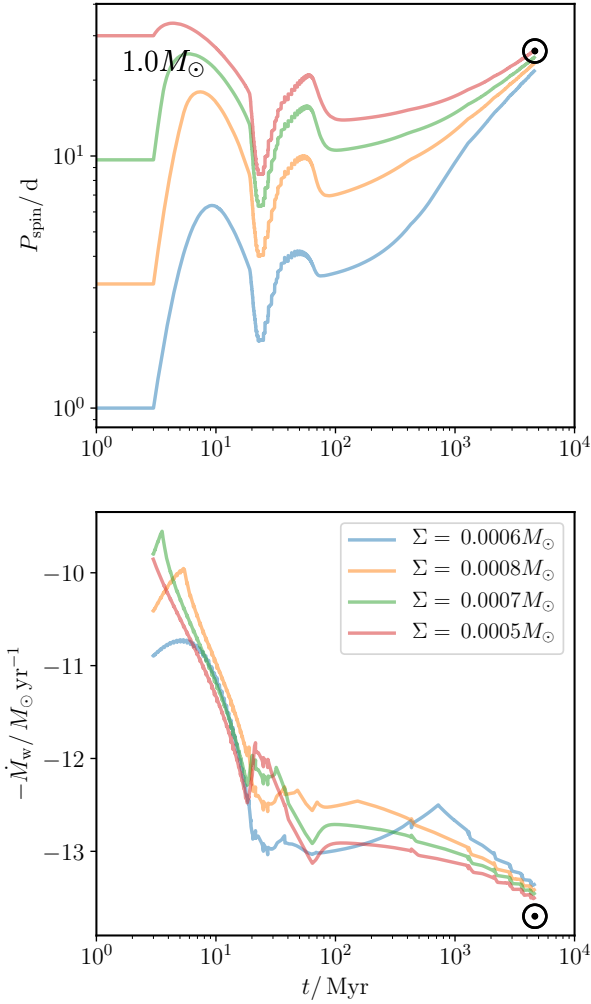


Figure 8. The evolution of the surface spin P_{spin} and mass-loss rate \dot{M}_w with time for a $1M_{\odot}$ star with $\tau_{\text{dl}} = 3$ Myr, initial $P_{\text{spin}} \in [1, 30]$ d equally spaced logarithmically. The free parameters are the same as in Fig. 7 and Σ denotes the total mass lost between τ_{dl} and t_0 .

with changes that incorporate the fact that the star is partly convective (Fig. 1). Our expression for the shear is from Zangrilli et al. (1997). We have also made additional modifications to the expressions for wind mass loss and Alfvén radius which influence MB (Table 3).

(iii) We work with three free parameters: our f_{shear} governs the efficiency of shear; f_2 marks the transition of the MB torque from the saturated ($\dot{J} \propto \Omega$) to the unsaturated ($\dot{J} \propto \Omega^3$) regime; and δ governs the behaviour of the wind-emitting surface of the star. The first parameter governs the strength of shear while the latter two govern the MB strength.

(iv) We use two coupled ordinary differential equations to solve the spins of the cores and the envelopes of a PCD from the time of its disc-dispersal to the end of the main sequence or the Galactic Age, whichever is earlier.

We arrive at several important conclusions.

(i) Our spin trajectories depend weakly on the strength of shear, with the dependence becoming weaker as the star attains a stable configuration after the pre-main sequence contraction phase. On the other hand, our spin trajectories strongly depend on the behaviour of the MB torque. We illustrate this by changing f_2 and δ .

(ii) The most massive FCMDs ($M_* \approx 0.35M_{\odot}$) experience stronger MB torques than less massive FCMDs ($M_* \lesssim 0.35M_{\odot}$) and more massive PCDs (Figs 6 and A1). These stars experience the strongest MB torque throughout and spin down the most within the Galactic Age.

(iii) Slow-rotating stars with masses between about $0.5M_{\odot}$ and $0.8M_{\odot}$ show a mass-dependent duration of stalled spin-down or minor spin-up (Fig. 6) such that less massive PCDs show a longer duration of stalling and at later times. Although the spin period at which this happens depends on the MB strength (Figs 4 and 5), its duration only weakly depends on MB and shear and is strongly stellar-structure-dependent. Our models show that a temporary epoch of stalled spin-down in K-dwarfs (Curtis et al. 2019; Curtis et al. 2020) is likely a MB- and stellar-structure dependent effect. Such a MB-dependent effect also simultaneously explains why these K-dwarfs are observed to be unusually active (Cao et al. 2023). This is because in K-stars there is a maximum in the wind mass-loss rate at P_{spin} between 15 and 20 d which is where the MB transitions from the saturated to the unsaturated regime (Fig. 7 and equation 11). Using wind mass loss as a proxy for stellar activity, we argue that this maximum in an otherwise smooth magnetic field and Alfvén radius profile can explain the unusual activity of such stars.

(iv) The pileup in the spin-mass plane observed by David et al. (2022) for massive PCDs ($M_* \gtrsim 1.0M_{\odot}$) is also reflected in our trajectories of $1.0M_{\odot}$ and $1.1M_{\odot}$ stars, wherein slow rotators experience weakened MB torques after Gyr time-scales. This is in accordance with the weakened magnetic braking paradigm proposed by van Saders et al. (2019). However, our fast rotators also transition from spin periods of a few to about 10 d. This is likely a dead-zone-dependent effect (fig. 4 of Sarkar et al. 2023c).

(v) The stalling of spin-down and unusual activity of K-dwarfs, and the pileups of G-dwarfs are unlikely to be the result of core-envelope coupling effects. For K-dwarfs, this is because the spin-stalling in our modelled stars only weakly depends on the efficiency of shear and the differential rotation required to explain the activity of K-dwarfs by shear-enhanced activity disagrees with our differential rotation estimates. The pileups of G-dwarfs cannot be explained by core-envelope coupling effects because such stars have corotating cores and envelopes at about 50 Myr, which is very early compared to the observed pileups at a few Gyr.

(vi) It is difficult to define a core-envelope corotation or coupling time-scale τ_{couple} when the core and the envelope achieve near corotation. This is because the time at which differential rotation becomes negligible in a trajectory is not only mass- and spin-dependent, but also depends strongly on MB uncertainties (Fig 4 and 5). However, the time at which the core and the envelope commence converging to a common spin weakly depends on MB-uncertainties and shear and is a stellar-structure-dependent phenomenon. We find that the core-envelope convergence time-scale τ_{converge} can be empirically estimated by equation (41). This expression is valid for all PCDs and spin periods above breakup. We also find that for fast rotators $\tau_{\text{couple}} \approx \tau_{\text{converge}}$.

(vii) We track the evolution of other observable parameters such as wind mass-loss rate, dipole component of the surface poloidal magnetic field B_p and the Alfvén radius and compare with observations. We find that our estimates agree better for around $1M_{\odot}$ stars and at longer periods. We also show that our model predicts weak, solar-like winds from young, rapidly rotating solar analogs which can explain the weak winds observed in a young, rapidly rotating solar analog star π^1 UMa. We see that our B_p estimates are the most robust. We find that these can be encapsulated within a factor of a few by an empirical expression given by equation (45).

(viii) We assess the validity of the massive young Sun hypothesis (Minton & Malhotra 2007) as a solution to the faint young Sun problem. This theory states that the Sun was born about 3 percent more massive than it is now, and that wind mass loss in the first few Gyr combined with luminosity increase as the Sun crosses the main sequence kept the early Earth's temperature warm enough for water to exist as liquid. We test this hypothesis with our wind mass-loss model and find that the maximum cumulative mass loss our Sun could have experienced is about $0.001M_{\odot}$, which is an order of magnitude lower than the minimum required to explain the problem with this theory. Thus, our model predicts that the massive young Sun theory is an unlikely solution to the faint young Sun problem.

ACKNOWLEDGEMENTS

AS thanks the Gates Cambridge Trust for his scholarship. AS thanks Jim Fuller for suggesting to undertake this work, as well as discussions on the spin evolution of low-mass stars. AS thanks Eric Blackman for insightful discussions on possible extensions of this work. CAT thanks Churchill College for his fellowship. AS and CAT thank James Pringle for drawing our attention to the faint young Sun problem.

DATA AVAILABILITY

No new data were generated in support of this research. Any numerical codes and related data generated during the work will be made available whenever requested by readers.

REFERENCES

- Barnes S. A., 2003, *ApJ*, **586**, 464
 Basu S., Antia H. M., 2003, *ApJ*, **585**, 553
 Bétrisey J., Eggenberger P., Buldgen G., Benomar O., Bazot M., 2023, *A&A*, **673**, L11
 Blackman E. G., Owen J. E., 2016, *MNRAS*, **458**, 1548
 Brown T. M., 2014, *ApJ*, **789**, 101
 Campbell C. G., Papaloizou J., 1983, *MNRAS*, **204**, 433
 Cao L., Pinsonneault M. H., van Saders J. L., 2023, *ApJ*, **951**, L49
 Cowling T. G., 1981, *ARA&A*, **19**, 115
 Curtis J. L., Agüeros M. A., Douglas S. T., Meibom S., 2019, *ApJ*, **879**, 49
 Curtis J. L., et al., 2020, *ApJ*, **904**, 140
 David T. J., Angus R., Curtis J. L., van Saders J. L., Colman I. L., Contardo G., Lu Y., Zinn J. C., 2022, *ApJ*, **933**, 114
 Denissenkov P. A., Pinsonneault M., 2007, *ApJ*, **655**, 1157
 Denissenkov P. A., Pinsonneault M., Terndrup D. M., Newsham G., 2010, *ApJ*, **716**, 1269
 Eggenberger P., Buldgen G., Salmon S. J. A. J., 2019, *A&A*, **626**, L1
 Eggenberger P., Buldgen G., Salmon S. J. A. J., Noels A., Grevesse N., Asplund M., 2022, *Nature Astronomy*, **6**, 788
 Eggleton P. P., 1973, *MNRAS*, **163**, 279
 Feulner G., 2012, *Reviews of Geophysics*, **50**
 Garraffo C., Drake J. J., Cohen O., 2015, *ApJ*, **813**, 40
 Garraffo C., Drake J. J., Cohen O., 2016, *A&A*, **595**, A110
 Garraffo C., et al., 2018, *ApJ*, **862**, 90
 Godoy-Rivera D., Pinsonneault M. H., Rebull L. M., 2021, *ApJS*, **257**, 46
 Jao W.-C., Henry T. J., White R. J., Nisak A. H., Hubbard-James H.-S., Paredes L. A., Lewis V. B., 2023, *AJ*, **166**, 63
 Johnstone C. P., Güdel M., 2015, *A&A*, **578**, A129
 Kawaler S. D., 1988, *ApJ*, **333**, 236
 Lanzafame A. C., Spada F., 2015, *A&A*, **584**, A30
 Lu Y. L., See V., Amard L., Angus R., Matt S. P., 2023, *Nature Astronomy*,

- MacGregor K. B., Brenner M., 1991, *ApJ*, **376**, 204
 Matt S. P., Brun A. S., Baraffe I., Bouvier J., Chabrier G., 2015, *ApJ*, **799**, L23
 Mestel L., Spruit H. C., 1987, *MNRAS*, **226**, 57 (MS)
 Metcalfe T. S., et al., 2022, *ApJ*, **933**, L17
 Metcalfe T. S., et al., 2023, *ApJ*, **948**, L6
 Minton D. A., Malhotra R., 2007, *AJ*, **660**, 1700–1706
 Parker E. N., 1955, *ApJ*, **122**, 293
 Pass E. K., Charbonneau D., Irwin J. M., Winters J. G., 2022, *ApJ*, **936**, 109
 Pavlov A. A., Kasting J. F., Brown L. L., Rages K. A., Freedman R., 2000, *Journal of Geophysical Research: Planets*, **105**, 11981–11990
 Pols O. R., Tout C. A., Eggleton P. P., Han Z., 1995, *MNRAS*, **274**, 964
 Rebull L. M., Wolff S. C., Strom S. E., 2004, *AJ*, **127**, 1029
 Regős E., Tout C. A., 1995, *MNRAS*, **273**, 146
 Rosing M. T., Bird D. K., Sleep N. H., Bjerrum C. J., 2010, *Nature*, **464**, 744
 Sadeghi Ardestani L., Guillot T., Morel P., 2017, *MNRAS*, **472**, 2590–2607
 Sarkar A., Tout C. A., 2022, *MNRAS*, **513**, 4169
 Sarkar A., Ge H., Tout C. A., 2023a, *MNRAS*, **519**, 2567
 Sarkar A., Ge H., Tout C. A., 2023b, *MNRAS*, **520**, 3187
 Sarkar A., Yungelson L., Tout C. A., 2023c, *MNRAS*, **526**, 870 (SYT I)
 Schatzman E., 1962, *Annales d'Astrophysique*, **25**, 18
 Shaviv N. J., 2003, *Journal of Geophysical Research (Space Physics)*, **108**, 1437
 Sills A., Pinsonneault M. H., Terndrup D. M., 2000, *ApJ*, **534**, 335
 Skumanich A., 1972, *ApJ*, **171**, 565
 Spada F., Lanzafame A. C., 2020, *A&A*, **636**, A76
 Spruit H. C., 2002, *A&A*, **381**, 923
 Thompson M. J., Christensen-Dalsgaard J., Miesch M. S., Toomre J., 2003, *Annual Review of Astronomy and Astrophysics*, **41**, 599–643
 Tout C. A., Pringle J. E., 1992, *MNRAS*, **256**, 269
 Verbunt F., Zwaan C., 1981, *A&A*, **100**, L7
 Villarreal D'Angelo C., Jardine M., See V., 2018, *MNRAS*, **475**, L25
 Warner B., 2003, *Cataclysmic Variable Stars*. Cambridge University Press, doi:10.1017/CBO9780511586491
 Wickramasinghe D. T., Tout C. A., Ferrario L., 2013, *MNRAS*, **437**, 675
 Wood B. E., Müller H.-R., Redfield S., Edelman E., 2014, *ApJ*, **781**, L33
 Wright N. J., Drake J. J., Mamajek E. E., Henry G. W., 2011, *ApJ*, **743**, 48
 Zahn J. P., 1992, *A&A*, **265**, 115
 Zangrilli L., Tout C. A., Bianchini A., 1997, *MNRAS*, **289**, 59
 van Saders J. L., Pinsonneault M. H., Barbieri M., 2019, *ApJ*, **872**, 128

APPENDIX A: EVOLUTION OF FULLY CONVECTIVE M-DWARFS

For the sake of completeness, we plot the spin-evolution of FCMDs with our MB model in Fig. A1. These stars have no radiative cores so our plots show the cores and the envelopes corotating at all times. The trajectories deviate from those of SYT I for low-mass FCMDs because of our additional implementation of the factor $(M_*/M_{\odot})^{-0.25}$ in equation (7) and calibrating $f_1 = 0.115$ (in SYT I it was a free parameter equal to 1.5).

APPENDIX B: EVOLUTION OF DIFFERENTIAL ROTATION DUE TO SHEAR

We plot the absolute relative differential rotation at the core-envelope boundary $\Delta\Omega_{\text{shear}}/\Omega_{\text{env}}$ in Fig. B1. Owing to rapid changes in the structure of the star, we see some stiffness in $\Delta\Omega_{\text{shear}}/\Omega_{\text{env}}$ at early times before the star becomes structurally stable. Beyond this, $\Delta\Omega_{\text{shear}}/\Omega_{\text{env}}$ decreases abruptly. We define this age as τ_{converge} in equation (41). We see a local maximum in $\Delta\Omega_{\text{shear}}/\Omega_{\text{env}}$ after Gyr in fast-rotating K-dwarfs. This can be alleviated by using a larger f_{shear} without changing any conclusion significantly (see Fig. 3 for a weak dependence on shear).

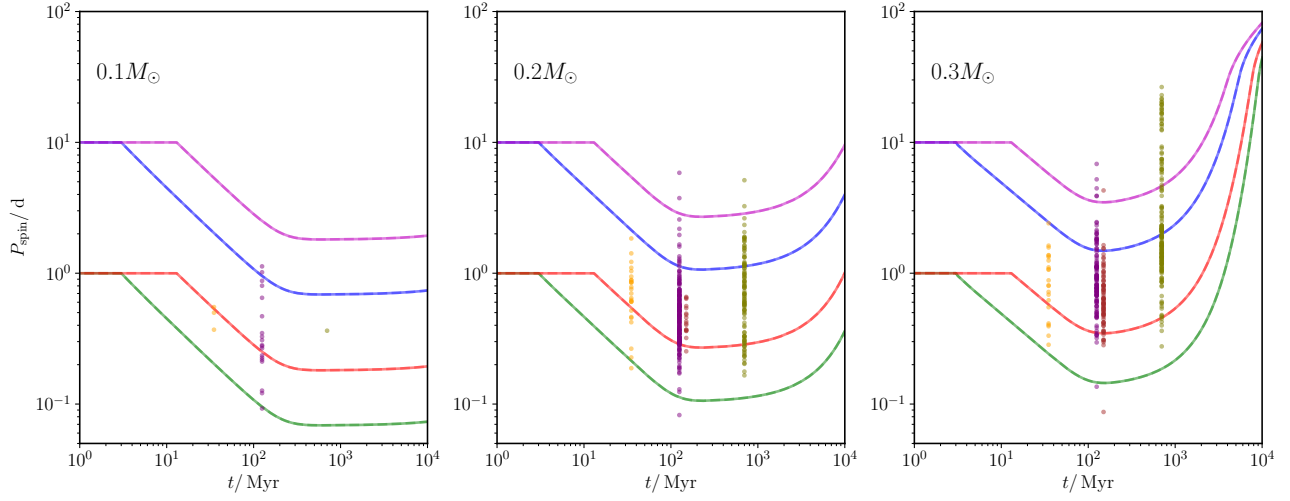


Figure A1. The evolution of P_{spin} with time for FCMDs with $\tau_{\text{dl}} \in \{3, 13\}$ Myr, $f_2 = 2$, $f_{\text{shear}} = 0.3$ and $\delta = 3$ with the same observations as in Fig. 5.

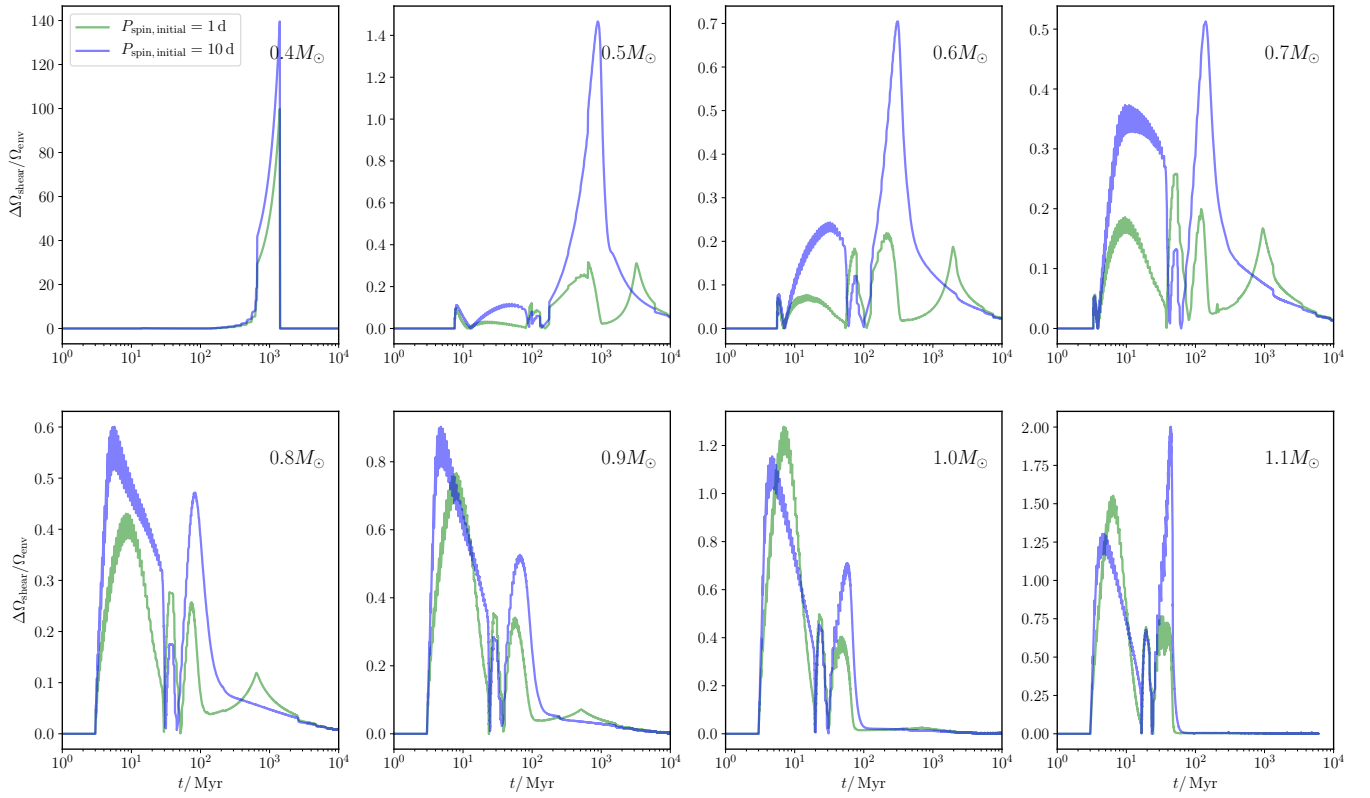


Figure B1. The evolution of $\Delta\Omega_{\text{shear}}/\Omega_{\text{env}}$ with time for various PCDs with $\tau_{\text{dl}} = 3$ Myr, $f_2 = 2$, $f_{\text{shear}} = 0.3$ and $\delta = 3$. Erratic behaviour is because $\Delta\Omega_{\text{shear}}/\Omega_{\text{env}}$ is stiff for PCDs at early times before the star transitions from its PMS phase to the MS phase (see Fig. 7).

This paper has been typeset from a \LaTeX file prepared by the author.